Paper published by Automatica, 2008, Vol. 44, p. 1766-1780.

Drag-Free and Attitude Control for the GOCE satellite

Enrico Canuto[*a]

[*] Corresponding author. Phone +39 011 564 7026 Fax +30 011 564 7198
[a] Politecnico di Torino, Dipartimento di Automatica e Informatica, Corso Duca degli Abruzzi 24, 10129 Torino, Italy
e-mail: enrico.canuto@polito.it

Abstract

The paper concerns Drag-Free and Attitude Control of the European satellite Gravity field and steady-state Ocean Circulation Explorer (GOCE) during the science phase. Design has followed Embedded Model Control, where a spacecraft/environment discrete-time model becomes the real-time control core and is interfaced to actuators and sensors via tuneable feedback laws. Drag-free control implies cancelling non-gravitational forces and all torques, leaving the satellite to free fall subject only to gravity. In addition, for reasons of science, the spacecraft must be carefully aligned to the local orbital frame, retrieved from range and rate of a Global Positioning System receiver. Accurate drag-free and attitude control requires proportional and low-noise thrusting, which in turn raises the problem of propellant saving. Six-axis drag-free control is driven by accurate acceleration measurements provided by the mission payload. Their angular components must be combined with the star-tracker attitude so as to compensate accelerometer drift. Simulated results are presented and discussed.

Key words: **satellite, drag-free, attitude, control, Embedded Model**.

1. Introduction

The Gravity field and steady-state Ocean Circulation Explorer (GOCE) satellite, to be launched in spring 2008, is part of the European space program dedicated to exploring the Earth's gravity field (Aguirre-Martinez & Cesare, 1999). The GOCE satellite will fly in a near-circular, sun-synchronous, dawn-dusk orbit (96.5° inclination) at a mean geodetic height $h \cong 250$ km, corresponding to the orbital rate $\omega_O \approx 1.17 \cdot 10^{-3}$ rad/s. At this altitude, drag effects are still significant due to the thermosphere (Section 1.1.2), which is a major control problem.

Spacecraft and control design are driven by three main concepts.

1) Gravity gradiometry. An on-board electrostatic gradiometer measures the gravity gradient from the linear combination of differential accelerations provided by six three-axis accelerometers (Touboul, Rodrigues, Willemenot & Bernard, 1996). Due to accelerometer drift (see Fig. 6 and Section 1.1.2), only small-scale spatial components of the gravity field can be recovered, leading to the mission (measurement) bandwidth :

$$\mathcal{F}_1 = \{ f_1 = 0.005 \le f \le f_2 = 0.1 \text{ Hz} \} . \quad (1)$$

Drag-free control derives from the need to cancel non-gravitational linear accelerations and angular accelerations in this region, so as to bound systematic instrument errors.

2) Orbit determination by satellite-to-satellite tracking. To recover the large-scale components of the gravity field, gradiometry must be complemented by precise satellite orbit. To this end, a Global Positioning System (GPS) receiver is embarked; GPS range and rate are also employed to estimate the reference attitude in real time, the so-called Local Orbital Reference Frame (LORF), prescribed by the instantaneous orbit (Section 2). Since gravity measurements will be referred to this frame, attitude control must accurately align the spacecraft to the orbital frame. The relevant pointing accuracy is tight within the mission frequency band, but rather loose at lower frequencies.
3) Drag-Free and Attitude Control (DFAC). Drag-free control at low altitudes requires low-noise proportional thrusters capable of tens of mN and with a time response shorter than 0.1 s. Attitude control is more stringent, calling for micro-thrusters having noise close to 1 μN and range below 1 mN. Proportional thrusting may raise the problem of propellant saving, micro-propulsion that of thrust peak restraint (Section 5.2). Micro-propulsion derives from the need of cancelling angular accelerations, from aerodynamic to gravity-gradient, in the mission bandwidth. To be accurate, angular drag-free control must be driven by gradiometer measurements that, being affected by bias, tend to cause attitude drifting. The gradiometer must be complemented by a star-tracker quaternion so as to align the spacecraft to the orbital frame. Attitude and angular acceleration estimation becomes a sensor fusion prob-

lem to be solved by careful noise design (Canuto, 2010).

The design of the GOCE drag-free and attitude control has followed the Embedded Model Control inspired by Donati & Vallauri (1984) and developed by Canuto (2007a). Embedded Model Control is not intended to improve performance over that of other techniques, but to equalise design, implementation and maintenance, a goal that is pursued by embedding the design model, thus known as an Embedded Model (EM), into the control unit (Section 3). Thus: (i) control design is done in the discrete-time domain (Section 4), (ii) the Embedded Model becomes the real-time plant image driven by commands and by accurate, up-to-date disturbance realizations (Sections 3.3 and 3.4), which are essential in drag-free control, (iii) the model error, the difference between plant measures and model output, is an explicit control signal and the sole source of feedback from plant to model, allowing real-time disturbance update through noise (Section 4.3). Control design is thus concerned with the following EM-to-plant interfaces.

1) The Control Law (Section 4.2) computes the digital commands one-step ahead as a combination of tracking errors and disturbances to be rejected.
2) The Noise Estimator (Section 4.3) estimates the driving noise capable of updating disturbance realizations.
3) The Reference Generator (Section 4.3) estimates the LORF quaternion as the attitude reference.

Control parameters either derive univocally from the Embedded Model itself or from the closed-loop eigenvalues, which result from closing Noise Estimator (output-to-state feedback) and Control Law (state-to-command feedback) on the model. As such, they are easily related to Embedded Model parameters, robust stability and performance (Section 4.4). The ensemble comprising the Embedded Model and the Noise Estimator constitutes a closed-loop state predictor. Eigenvalue design and tuning is first done by analytic techniques and then refined through simulation and in field during commissioning. In this respect, the architecture of the Embedded Model Control looks rather similar to Linear Quadratic Gaussian (LQG) architecture, but no optimization is explicitly sought and state-predictor eigenvalues are designed with respect to neglected dynamics, so as to recover model-based stability and performance (Section 4.4).

Drag-free control has mostly been designed in the frequency domain using H_∞ techniques (Vaillon, Borde, Duhamel & Damilano, 1996, Ziegler & Blanke, 2002, Fichter, Gath, Vitale & Bartoluzzi, 2005). First of all, the design model is decoupled as far as possible, thus neglecting cross-couplings or treating them as unknown disturbance, unlike Embedded Model Control in which they are accurately modelled and cancelled if significant to stability and performance. Mixed sensitivity inequalities are then established for each degree of freedom, with the help of disturbance shaping filters and performance templates. The resulting controllers look blind with respect to the model and requirements, hence are not easily adjustable. Further obscurity may come from conversion into digital filters for coding. Controllers are never reported, nor is the design model distinguished from the fine model, so as to account for neglected dynamics. LQG design, endowed with the explicit model of a harmonic disturbance, is reported by Vaillon, Borde, Duhamel & Damilano (1996), who account for precautions in converting to digital filters and mention the difficulty of guaranteeing robust stability, mainly because of solar panel vibrations close to the control bandwidth. Simple PID laws lacking explicit disturbance rejection have been treated by Haines (2000). Model predictive control has been proposed by Prieto & Ahmad (2005) for treating propellant saving, but through quadratic cost. Some of the cited papers refer to GOCE, but comparison is awkward due to a lack of details about simulation and control algorithms. On the contrary, the orbit and attitude simulator developed for the purpose by the author was so effective that the control code transported to the end-to-end GOCE simulator provided the same performance, and constituted the prototype for final code development.

Reference frames and control requirements are presented in Section 2. The Embedded Model is derived in Section 3, briefly justifying simplifications with respect to the simulated fine model. Care is devoted to disturbance dynamics as a way to squeeze an accurate and timely perturbation state from the measurements, ready to be counteracted by drag-free control. Actuator and sensor dynamics are briefly mentioned as they contribute to neglected dynamics. Section 4 provides an overview of the relevant digital control. Simulated results and discussion are given in Section 5.

2. Reference frames and DFAC requirements

The main GOCE frame is the Local Orbital Reference Frame $\mathcal{R}_O = \{C, \mathbf{i}_O, \mathbf{j}_O, \mathbf{k}_O\}$, which is defined (i) by the motion direction $\mathbf{v}/V$ of the spacecraft Centre-of-Mass (CoM), where $\mathbf{v}$ is the inertial velocity and $V = |\mathbf{v}|$ the velocity amplitude, and (ii) by the orbital plane orthogonal to the angular momentum $\mathbf{h} = m_s \mathbf{r} \times \mathbf{v}$, where $m_s \simeq 1080$ kg denotes the spacecraft mass and $\mathbf{r}$ the centre-of-mass position (Fig. 1). The origin C coincides with the satellite CoM, while the LORF axes are defined by:

$$\begin{aligned} &\mathbf{i}_O = \mathbf{v}/V, \mathbf{j}_O = \mathbf{r} \times \mathbf{v} / |\mathbf{r} \times \mathbf{v}|, \mathbf{k}_O = \mathbf{i}_O \times \mathbf{j}_O \\ &V \simeq (r_E + h)\omega_O \simeq 7760 \text{ m/s}, r_E \simeq 6.380 \times 10^6 \text{ m} \end{aligned}, \tag{2}$$

where ω_O is the instantaneous orbital rate defined by

$$\omega_O = |\mathbf{r} \times \mathbf{v}| / |\mathbf{r}|^2 . \tag{3}$$

The axes, ordered from $\mathbf{i}_O$ to $\mathbf{k}_O$, are referred to as along-track, out-of-plane and radial, respectively. The matrix $R_O(\mathbf{r}, \mathbf{v}) = [\mathbf{i}_O \quad \mathbf{j}_O \quad \mathbf{k}_O]$, i.e. the LORF-to-inertial-frame transformation, defines the reference quaternion $\mathcal{Q}_O$ to be tracked by the spacecraft attitude quaternion $\mathcal{Q}$.

The body frame $\mathcal{R} = \{C, \mathbf{i}, \mathbf{j}, \mathbf{k}\}$ is imposed by the geometry and mass distribution of the spacecraft, which has a slender cylindrical body (Fig. 2). The cylinder length is 4.9 m and the cross-section area is 0.65 m^2. The body unit vectors are quasi-aligned with the principal axes of

inertia, and $\mathbf{i}$, aligned with the cylinder axis, points toward $\mathbf{v}$.

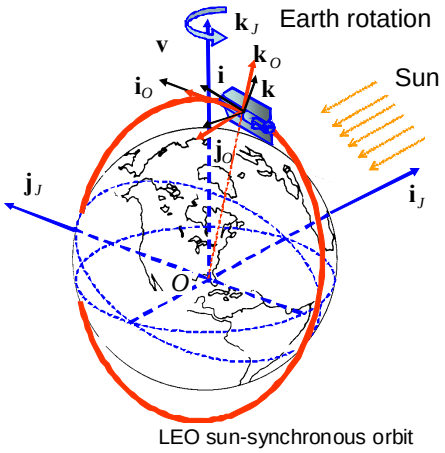

Fig. 1 Main reference frames of the GOCE satellite in a dawn-dusk orbit (orbit and spacecraft are not in scale).

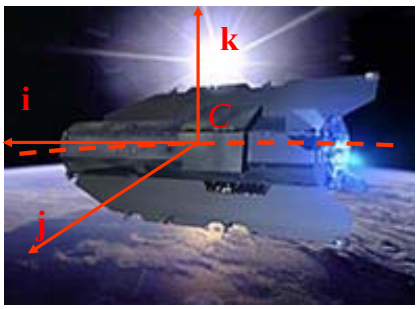

Fig. 2 Artist's view of the GOCE satellite in a dawn-dusk orbit.

Modelling and control design assumes attitude control to keep the inertial attitude quaternion $\mathcal{Q}$ aligned with the reference quaternion $\mathcal{Q}_O$ less a few milliradians. Accordingly, the attitude vector $\mathbf{q}=\{q_x,q_y,q_z\}$ is defined as the vector of the Euler angles entering the body-to-LORF transformation

$$R(\mathbf{q})=Z(q_z)Y(q_y)X(q_x). \tag{4}$$

where $X(q_x)$, $Y(q_y)$ and $Z(q_z)$ denote roll, pitch and yaw rotation matrices, respectively.

Control requirements are defined in terms of the following performance variables:

1) the residual non-gravitational acceleration $\mathbf{a}_I$ of the spacecraft centre-of-mass, in body coordinates,
2) the satellite angular acceleration $\mathbf{a}_q=\dot{\boldsymbol{\omega}}$,
3) the misalignment between the body frame $\mathcal{R}$ and the orbital frame $\mathcal{R}_O$, expressed by the attitude $\mathbf{q}$ and the rate

$$\Delta\boldsymbol{\omega}=\boldsymbol{\omega}-R^T(\mathbf{q})\omega_O\mathbf{j}_O, \tag{5}$$

where $\boldsymbol{\omega}=\{\omega_x,\omega_y,\omega_z\}$ is the inertial angular rate in body coordinates.

Drag-free and attitude zero tracking are expressed by

$$\underline{\mathbf{a}}_I=0,\ \underline{\mathbf{a}}_q=0,\ \underline{\Delta\boldsymbol{\omega}}=0,\ \underline{\mathbf{q}}=0, \tag{6}$$

where underline denotes reference values.

Equation (6) clarifies a key difference.

1) Centre-of-mass motion has to be free falling, i.e. only forced by gravity, which implies no control requirement on position $\mathbf{r}$ and rate $\mathbf{v}$. Only the non-gravitational acceleration $\mathbf{a}_I$ must be controlled to zero, which is referred to as pure drag-free.
2) Attitude control, taking advantage of acceleration (gradiometer) and attitude sensors (star tracker), can be broken down hierarchically into (i) drag-free control, as for the centre-of-mass, having a larger bandwidth (BW) to cancel drag and gravity torques, and (ii) attitude control, having a narrower bandwidth but sufficient to cancel the gradiometer drift $\mathbf{b}_a$, and to keep attitude and rate bounded. Hence, the angular acceleration $\mathbf{a}_a$ including the gradiometer drift $\mathbf{b}_a$ must be distinguished from the attitude acceleration $\mathbf{a}_q$, free of drift and defined by $\mathbf{a}_q=\mathbf{a}_a+\mathbf{d}_q$, where $\mathbf{d}_q=-\mathbf{b}_a$ must be cancelled by attitude control.

Control requirements on tracking errors are shown in Table 1. They are not uniform within the control frequency band $\mathcal{F}_c$ ranging from DC to Nyquist frequency $f_{\max}=0.5/T=5$ Hz, where $T=0.1$ s is the control time unit. Requirements are stringent in the mission bandwidth defined in (1), but more relaxed in the lower-frequency region $\mathcal{F}_0=\{f\le f_1\}$ and in the higher-frequency region $\mathcal{F}_2=\{f_2\le f\le f_{\max}\}$. Spectral density bounds in Table 1 are completed with a root-mean-square (RMS) bound.

Table 1. GOCE drag-free and attitude requirements

Variable	Unit	$\mathcal{F}_0$	$\mathcal{F}_1$	$\mathcal{F}_2$
Spectral density upper bounds				
$\mathbf{a}$	$\mu m/\left(s^2\sqrt{Hz}\right)$	35	0.025	0.2
$\dot{\boldsymbol{\omega}}$	$\mu rad/\left(s^2\sqrt{Hz}\right)$	70	0.025	0.025
$\Delta\boldsymbol{\omega}$	$\mu rad/\left(s\sqrt{Hz}\right)$	700	0.5	NA
$\mathbf{q}$	$mrad/\sqrt{Hz}$	26	0.008	NA
RMS upper bound				
$\mathbf{a}$	$\mu m/s^2$	0.5		
$\dot{\boldsymbol{\omega}}$	$\mu rad/s^2$	1		
$\Delta\boldsymbol{\omega}$	$\mu rad/s$	10		
$\mathbf{q}$	μrad	0.37		

Further requirements come from micro-thruster technology: gas propulsion requires propellant saving, electric micro-thrusting may require peak restraining. Propellant saving can exploit micro-thruster redundancy, since they amount to $m=8$, a size greater than the total degrees-of-freedom $2n-1=5$ of lateral position and attitude. To this end, the l_1 norm of the commanded thrust vector $\mathbf{u}_m$, sized m, must be minimized at each control time i by solving

$$\begin{matrix} \min_{\mathbf{u}_m} \mathbf{e}^T \mathbf{u}_m(i),\ \mathbf{e}^T = [1 \quad \dots \quad 1] \\ B_m \mathbf{u}_m(i) = \mathbf{a}_m(i),\ \mathbf{u}_m(i) \geq 0 \end{matrix}, \tag{7}$$

where $\mathbf{a}_m$ is the vector of the commanded accelerations, lateral and angular, to be defined in Section 3.5, and B_m the relevant scale-factor matrix. Peak restraining, if formulated as a l_∞-norm minimization, a subject not treated here, would become an alternative to propellant saving. Actually, a more sophisticated approach was applied as outlined in Section 5.2.

3. From fine to Embedded Model

3.1. Introduction

Embedded Model Control distinguishes between the fine model to be implemented as a numerical simulator for control assessment, and the Embedded Model, the stylized model part of the control unit. Discrepancies between fine and Embedded Model are essential, as they fix the simplifying assumptions separating modelled and neglected dynamics. Control laws descend from the Embedded Model, but closed-loop eigenvalues are tuned versus requirements and neglected dynamics.

This section focuses on the Embedded Model, neglecting fine-model design. Actually, fine model complexity must be carefully designed to enhance model discrepancies with respect to the Embedded Model. For instance, consider milliradian attitude accuracy, as reported in Table 1, and the relevant zero reference in (6). This would suggest adopting linearized attitude dynamics for both the fine and the Embedded Model. In practice this would imply neglecting square terms of the order of 10^{-6}, which is the same magnitude of the requirement in Table 1, in the column labelled $\mathcal{F}_1$. The fine attitude must thus be non-linear or expanded up to second-order terms, while the Embedded Model is linear, discrepancies being accommodated by a careful modelling of the unknown perturbations. Similar considerations apply to cross-coupling terms and attitude-dependent torques, such as aerodynamic and gravity-gradient. Last but not least, the high-frequency dynamics due to sensors and actuators, having time constants and natural frequencies close to control time unit T - taken as the EM time unit - become an essential part of the fine model and the main candidates to neglected dynamics.

The above considerations fix the pathway from fine to Embedded Model.

1) The controllable/observable part of the fine model is simplified by neglecting: (i) cross-coupling and internal feedback, treated as unknown/known perturbations to be explicitly cancelled if significant; (ii) the high-frequency dynamics, whose effect, although excited by commands, remains within a tolerance compatible with control requirements.
2) Disturbance and cross-couplings split into known and unknown terms. A class of unknown, observable disturbances is then synthesized, capable of encompassing the expected realizations to be counteracted within the target tolerance. Each class is synthesized as the output of discrete-time, linear state equations driven by a noise vector $\mathbf{w}$. Class complexity corresponds to equation order and descends from simulated/experimental spectral densities as in Fig. 5. As a baseline, no statistics are appended to $\mathbf{w}$, except for a priori performance assessment (Section 4.4), thus leaving $\mathbf{w}$ to be interpreted as a class of bounded and arbitrary signals, having asymptotic zero average and zero prediction. Moreover, by placing eigenvalues on the unit circle, wide, robust classes of random drifts can be synthesized, since they are parameter-free.
3) The Embedded Model is completed by an analytic model of the neglected dynamics and the relevant uncertainty range, not to be embedded but driving closed-loop eigenvalues. Details on neglected dynamics are omitted for brevity's sake.

3.2. Notations and block-diagram

Three sets of subscripts and two dimensional indices are employed.

1) The centre-of-mass (or attitude) subscript $c = x, y, z$, denotes either a generic axis, or the along-track (roll), out-of-orbit plane (pitch) and radial (yaw) axes, respectively;
2) The decomposition subscript $h = l, a, r, q$, either denotes a generic dynamics/variable or it is restricted to CoM acceleration, angular acceleration, CoM position and attitude, respectively;
3) The thruster subscripts t and m refer to ion thruster (along-track axis) and micro-thrusters (lateral axes and attitude), respectively, as explained in Section 3.5.
4) The micro-thruster size is $m = 8$ and the CoM/attitude degrees-of-freedom are $n = 3$.

Spacecraft dynamics is directly written in the discrete-time domain, using the $\mathcal{Z}$-transform notation, also when nonlinear, time-varying terms are involved. The notation $\mathbf{y}(z) = \mathbf{P}(z)\mathbf{u}(z)$ is simplified to $\mathbf{y} = \mathbf{P} \cdot \mathbf{u}$ when z is dropped. Note that the $\mathcal{Z}$ notation hides the initial state and free response, which would be made explicit by state equations, omitted for brevity's sake. Derivation from continuous-time dynamics is shown when necessary. The block-diagram of the Embedded Model is shown in Fig. 3 and corresponds to a set of discrete-time state equations driven by $m+1$ commands and ending in $5n$ measures. Clouds denote driving noise and express causal uncertainty. The open switch between thrust matrix B and orbit dynamics, points out that thrust command is not intended for orbit control, but just for making the orbit drag-free.

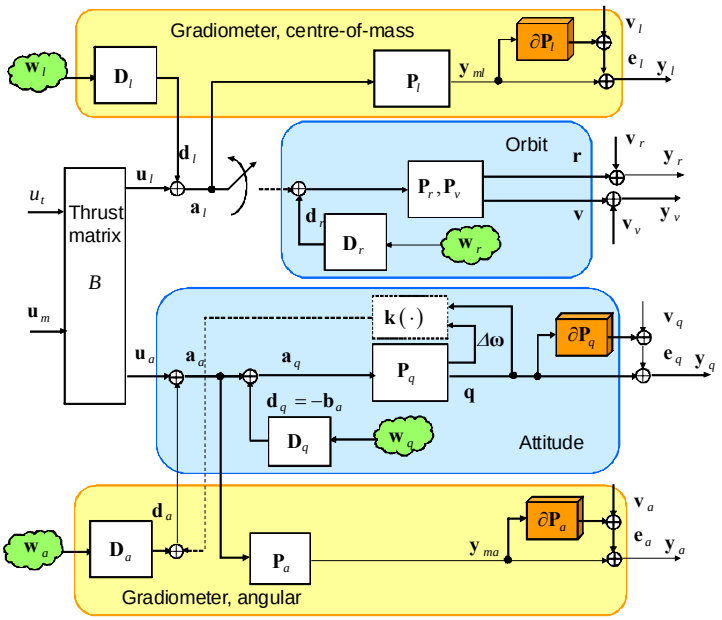

Fig. 3 Block-diagram of the Embedded Model.

3.3. *Centre-of-mass dynamics*

1.1.1. Inertial dynamics for LORF quaternion prediction

Centre-of-mass dynamics may be written either in inertial or body frame. Inertial equations, written in the Earth-centred equatorial frame $\{O,\mathbf{i}_J,\mathbf{j}_J,\mathbf{k}_J\}$ (see Fig. 1), are employed to filter GPS range and rate measurements in view of the orbital quaternion prediction (Canuto, Massotti & Santos, 2007). To this end, the Earth's gravity acceleration $\mathbf{g}(\mathbf{r})$ is explicitly modelled so as to include the Earth's oblateness term J2, as follows

$$\mathbf{g}(\mathbf{r}) \simeq -\underline{\omega}_O^2\left(1-\partial\Omega(\mathbf{r})\right)\mathbf{r}\,, \tag{8}$$

where $\underline{\omega}_O$ is the mean orbit rate and $|\partial\Omega(\mathbf{r})| \le 0.02$ accounts for eccentricity and J2. Deviation from the rule, given in Section 3.1, of treating internal feedback as a known disturbance is justified by the narrow bandwidth of the LORF predictor close to $\underline{\omega}_O$, and imposed by conservative GPS errors. Three weakly-coupled, time-varying oscillators are modelled, tuned on the discrete-time rate

$$\alpha_c(i) = \underline{\omega}_O T\sqrt{1-\partial\Omega(\mathbf{r})}\,, \tag{9}$$

and driven by drag-free residuals $\mathbf{d}_r$ which also account for gravity anomalies. No explicit command force is included since the orbit is drag-free, but the orbit is corrupted by the accelerometer drift being part of $\mathbf{d}_r$. Orbit dynamics is written as follows

$$\begin{bmatrix}\mathbf{r}\\ \mathbf{v}\end{bmatrix}(z) = \begin{bmatrix}\mathbf{P}_r\\ \mathbf{P}_v\end{bmatrix}(z)\mathbf{d}_r(z)\,, \tag{10}$$

upon definition of the $\mathcal{Z}$ transfer functions from acceleration to position

$$\mathbf{P}_r(z) = \mathrm{diag}\left\{\mathbf{P}_{rc}(z) = \frac{\sin\alpha_c}{\alpha_c\left(\left(z-\cos\alpha_c\right)^2+\sin^2\alpha_c\right)}\right\}, \tag{11}$$

and from acceleration to rate

$$\mathbf{P}_v(z) = \mathrm{diag}\left\{\mathbf{P}_{vc}(z) = \frac{z-\cos\alpha_c}{\left(\left(z-\cos\alpha_c\right)^2+\sin^2\alpha_c\right)}\right\}. \tag{12}$$

The unknown disturbance class includes first- and second-order random drift, to account for the spectral density of gravity anomalies rolling off at -40dB/dec in the band $f > 3\omega_O(2\pi)^{-1} \simeq 1$ mHz, which is referred to as Kaula's rule (Bertotti & Farinella, 1990). Restricting considerations to the generic component c, the transfer function from noise to disturbance reads

$$\begin{aligned} d_{rc}(z) &= \mathbf{D}_{rc}(z)\mathbf{w}_{rc}(z)\\ \mathbf{D}_{rc}(z) &= \begin{bmatrix}1 & (z-1)^{-1} & (z-1)^{-2}\end{bmatrix}. \end{aligned} \tag{13}$$

Equations (10) and (13) together with (2) and the GPS measurement equations

$$\begin{aligned} \mathbf{y}_r(z) &= \mathbf{r}(z)+\mathbf{v}_r(z)\\ \mathbf{y}_v(z) &= \mathbf{v}(z)+\mathbf{v}_v(z) \end{aligned}, \tag{14}$$

are the Embedded Model for the LORF state predictor. Although GPS data are provided at a lower rate, namely 1 Hz, and delayed, the LORF quaternion is extrapolated at

the DFAC rate $f_c = 1/T = 10$ Hz though a predictor-corrector algorithm (Canuto, Massotti & Santos, 2007). Properties of GPS measurement errors $\mathbf{v}_r$ and $\mathbf{v}_v$ are omitted (Kaplan, 1966), but they are stylized to be discrete-time, white and Gaussian noise, and their components to be statistically independent.

1.1.2. Non-gravitational acceleration dynamics and drag-free control

The drag-free control of the spacecraft centre-of-mass would in principle need body-frame equations relating the non-gravitational acceleration $\mathbf{a}_I$, measured by the gradiometer in body coordinates, to thruster commands. The complete equations, which are usually written in terms of the relative motion of the centre-of-mass with respect to an average circular orbit, are not reported here (Scheeres, 1998, Canuto, 2010). Here we are only interested in the non-gravitational acceleration $\mathbf{a}_I$ written as the sum of drag and thruster forces $\mathbf{f}_d$ and $\mathbf{f}$, as follows

$$\mathbf{a}_I(t) = \left(\mathbf{f}_d(\mathbf{r},\mathbf{v},\mathbf{q},t) + \mathbf{f}(t)\right)/m_s \,. \tag{15}$$

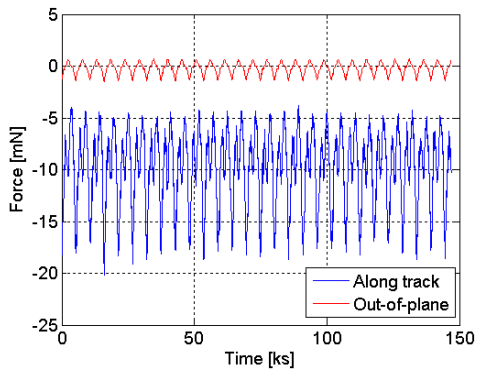

Fig. 4 Time history of along-track (bottom) and out-of-plane (top) drag.

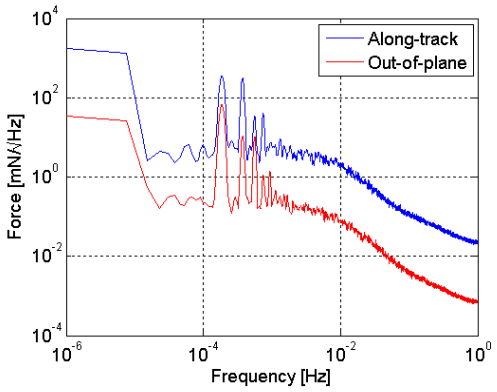

Fig. 5 Spectral density of along-track (top) and out-of-plane (bottom) drag.

At low altitudes, drag is dominated by aerodynamic forces; solar pressure and the Earth's radiation are much smaller. Although drag may be written as a known function of the spacecraft centre-of-mass and attitude (Wertz, 1985) as in (15), at least with regard to components close to the orbital period $T_O = 2\pi/\omega_O \simeq 5370$ s (see Fig. 4), the relevant scale factors are highly uncertain, complex random processes establish over shorter time scales than the mission bandwidth $\mathcal{F}_1$, and short-time drag variations may occur due to shadowing (Fritsche & Klinkrad, 2004). Being interested in time scales shorter than a second, standard thermosphere models limited to less than 0.1 Hz (Picone, Heidin, Drob & Aitken, 2002), were stochastically extrapolated to 10 Hz in agreement with high-frequency asymptotes of experimental spectral densities (Fig. 5). In addition, spectral analysis lead to a second-order disturbance class as in (13), since, for $f \geq 1$ mHz, spectral densities can be piecewise enveloped by $-(20 \div 40)$ dB/dec slope, as confirmed by Fig. 5. The combination of white noise, first- and second-order random drift defines a very wide class of signals, compatible with the large gradiometer bandwidth, thus removing the need for drag-explicit models in the control algorithms.

The Embedded Model must be completed with gradiometer/thruster dynamics and noise. Thruster dynamics and noise are briefly outlined in Section 3.5. Gradiometer dynamics is the cascade of servo-accelerometer dynamics (>20 Hz), anti-aliasing filter (close to $f_{\max}$) and data transmission delay (Canuto, Bona, Calafiore & Indri, 2002). Thruster-to-gradiometer dynamics is stylized by time delay, thus treating residual dynamics - mainly thruster and anti-aliasing filter - as neglected dynamics. Gradiometer noise, typical of servo-accelerometers, shows a spectral density reaching a minimum inside the mission bandwidth $\mathcal{F}_1$, while increasing at lower and higher frequencies as in Fig. 6. The higher-frequency 40dB/dec slope justifies anti-aliasing. The low frequency slope, corresponding to accelerometer drift and bias $\mathbf{b}_I$, falls into the second order disturbance class (13) adopted for the drag. The same holds for thruster noise.

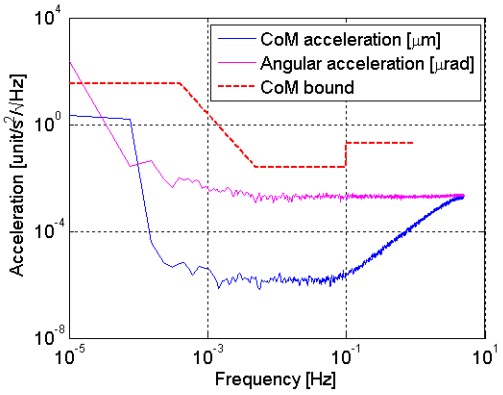

Fig. 6 Spectral densities of the gradiometer noise for CoM (bottom) and angular measurements (middle) compared to drag-free target bound (top).

The first step toward Embedded Model construction is the following $\mathcal{Z}$-transform equation

$$\begin{aligned} a_{Ic}(z) &= \mathbf{D}_{Ic}(z)\mathbf{w}_{Ic}(z) + B_{Ic}\mathbf{u}(z) \\ \mathbf{y}_I(z) &= \mathbf{P}_I(z)\left(\mathbf{a}_I(z) + \mathbf{b}_I(z)\right) + \mathbf{e}_I(z) \end{aligned}, \tag{16}$$

where $d_{lc} = \mathbf{D}_{lc} \cdot \mathbf{w}_{lc}$ and $\mathbf{D}_{lc}(z) = \mathbf{D}_{rc}(z)$ (see equation (13)) account for non-gravitational accelerations and thruster noise, $B_{lc}\mathbf{u}$ is the commanded acceleration to be explained in Section 3.5, and $\mathbf{y}_l$ is the gradiometer measurement which is affected by a delay denoted with

$$\mathbf{P}_l(z) = \mathrm{diag}\left\{\mathbf{P}_{lc}(z) = z^{-1}\right\}, \tag{17}$$

and is driven by the model error $\mathbf{e}_l$ and the drift $\mathbf{b}_l$. Then, upon definition of the error-free model output $\mathbf{y}_{ml} = \mathbf{P}_l \cdot (\mathbf{a}_l + \mathbf{b}_l)$, and inclusion of $\mathbf{b}_l$ into the unknown disturbance $\mathbf{d}_l$, the final EM follows

$$\begin{aligned} \mathbf{y}_{ml}(z) &= \mathbf{P}_l(z)\left(\mathbf{d}_l(z) + B_l\mathbf{u}(z)\right) \\ \mathbf{y}_l(z) &= \mathbf{y}_{ml}(z) + \mathbf{v}_l(z) + \partial\mathbf{P}_l(z)\mathbf{y}_{ml}(z) \end{aligned}. \tag{18}$$

In (18), the model output $\mathbf{y}_{ml}$ only accounts for the low-frequency component $\mathbf{d}_l$ to be rejected by the command $\mathbf{u}$ (drag-free control). The command necessarily includes the gradiometer drift, which in turn affects the spacecraft orbit outside the mission bandwidth but, being compatible with low-frequency requirements in Table 1, does not need to be rejected by a specific orbit control. On the contrary, the model error $\mathbf{e}_l$ refers (i) to middle-to-high frequency components $\mathbf{v}_l$ of the gradiometer noise, playing the role of measurement noise, and (ii) to the neglected dynamics $\partial\mathbf{P}_l \cdot \mathbf{y}_{ml}$, written in fractional form, i.e. driven by the model output $\mathbf{y}_{ml}$ (Canuto, 2007a). Neglected dynamics (sometimes referred to as unstructured uncertainty) is not part of the Embedded Model, but it is such as to constrain control performance (Section 1.1.8). The fractional form $\partial\mathbf{P}_l$ of the neglected dynamics in (18) is assumed to be stable, linear and time-invariant.

3.4. Attitude dynamics

1.1.3. Linearized dynamics

Restricting considerations to the Embedded Model, attitude kinematics is written in Euler angles, as coarse alignment is outside DFAC requirements (Canuto, Martella & Sechi, 2003). Then, linearizing around $\underline{\mathbf{q}}(t) = 0$ yields

$$\dot{\mathbf{q}}(t) = \boldsymbol{\omega}(t) - \omega_O\mathbf{j} = \Delta\boldsymbol{\omega}(t), \quad \mathbf{q}(0) = \mathbf{q}_0, \tag{19}$$

where $\Delta\boldsymbol{\omega} = \left\{\Delta\omega_x, \Delta\omega_y, \Delta\omega_z\right\}$ has been defined in (5), having assumed ω_O to be constant.

Attitude dynamics follows by linearizing the classical Euler equation around $\underline{\Delta\boldsymbol{\omega}}(t) = 0$, $\underline{\mathbf{q}}(t) = 0$, which leads to

$$\begin{aligned} &\Delta\dot{\boldsymbol{\omega}}(t) = A_\omega\Delta\boldsymbol{\omega}(t) + A_q\mathbf{q}(t) + \\ &+ J^{-1}\left(\mathbf{c}_d(\mathbf{q},\mathbf{r},\mathbf{v},t) + \mathbf{c}_m(\mathbf{q},\mathbf{r},t) + \mathbf{c}(t)\right). \\ &\Delta\boldsymbol{\omega}(0) = \Delta\boldsymbol{\omega}_0 \end{aligned} \tag{20}$$

The magnetic torque

$$\mathbf{c}_m(\mathbf{q},\mathbf{r}) = \mathbf{m}(t) \times \mathbf{b}_E(\mathbf{q},\mathbf{r}), \tag{21}$$

follows upon defining the Earth's magnetic field $\mathbf{b}_E$ and the spacecraft magnetic dipole moment $\mathbf{m}$, in body coordinates. Gyro and gravity-gradient matrices in (20) are defined as follows

$$A_\omega = \begin{bmatrix} 0 & 0 & \Omega_x \\ 0 & 0 & 0 \\ -\Omega_z & 0 & 0 \end{bmatrix}, \; A_q = \begin{bmatrix} -\Omega_{gx}^2 & -\Omega_{gxy}^2 & 0 \\ 0 & \Omega_{gy}^2 & 0 \\ 0 & 0 & 0 \end{bmatrix}. \tag{22}$$

The inertia tensor J is quasi-diagonal:

$$J = \begin{bmatrix} 153 & -23 & -6 \\ -23 & 2691 & 1 \\ -6 & 1 & 2653 \end{bmatrix} \mathrm{kgm}^2. \tag{23}$$

1) The first term in the right-hand side (RHS) of (20) is the linearized gyro acceleration, depending on the angular frequencies $\Omega_z \simeq \omega_O$ and $\Omega_x \simeq \omega_O / 4$. It is treated as a known disturbance to be cancelled, less a slight uncertainty, accommodated by unknown disturbance components.
2) The second RHS term in (20) is the linearized gravity–gradient acceleration, depending on the angular frequencies

$$\Omega_{gx} < \omega_O, \; \Omega_{gxy} < \omega_O, \; \Omega_{gy} \simeq \sqrt{3}\omega_O. \tag{24}$$

   The positive sign of Ω_{gy}^2 in (20) implies that the spacecraft pitch angle q_y is locally unstable, since the gravity gradient would tend to align the GOCE slender spacecraft to zenith/nadir. 'In the large', attitude has been made stable passively, i.e. by providing the spacecraft tail with suitable aerodynamic surfaces (see Fig. 2). Thanks to gradiometer bandwidth, the gravity gradient in (20) can be treated as a perturbation to be cancelled, either known or unknown, thus leaving attitude dynamics parameter-free but unstable.
3) The last terms in (20) correspond to the aerodynamic torque, $\mathbf{c}_d$, to the magnetic torque $\mathbf{c}_m$, and to the control torque $\mathbf{c}$, all written in body coordinates. Aerodynamic torques, although attitude-dependent, are treated as unknown perturbations as in (13) due to uncertain scale factors and short-time components. The same applies to the magnetic torque $\mathbf{c}_m$ because of the uncertain and variable spacecraft magnetic dipole moment $|\mathbf{m}(t)| \simeq 5 \div 10 \; \mathrm{Am}^2$.

1.1.4. Discrete-time dynamics

Similarly to the dynamics of the satellite centre-of-mass in Section 3.3, the Embedded Model is divided into attitude dynamics driven by residual angular acceleration $\mathbf{a}_a$ and acceleration dynamics. The latter includes the thruster-to-gradiometer dynamics approximated by a delay as in (17). Taking advantage of (19) and (20), attitude dynamics is simplified as follows.

1) Coordinate decomposition is exploited, leading to three independent and equal dynamics from residual acceleration $\mathbf{a}_a$ to attitude $\mathbf{q}$. Cross-coupling accelerations, namely gyro and gravity-gradient, are confined within acceleration dynamics.
2) The RHS in (20) is written as the sum of the residual acceleration $\mathbf{a}_a$, ideally zero, and the opposite of the

gradiometer bias $\mathbf{d}_q = -\mathbf{b}_a$. The latter is modelled by a second order random class as in (13), i.e. $d_{qc} = \mathbf{D}_{qc} \cdot \mathbf{w}_{qc}$ and , $\mathbf{D}_{qc}(z) = \mathbf{D}_{rc}(z)$.
The resulting attitude dynamics is

$$\begin{aligned} &\mathbf{q}(z) = \mathbf{P}_q(z)\left(\mathbf{a}_a(z) + \mathbf{d}_q(z)\right) = \mathbf{P}_q(z)\mathbf{a}_q(z) \\ &\mathbf{P}_q(z) = \mathrm{diag}\left\{\mathbf{P}_{qc}(z) = (z-1)^{-2}T^2\right\} \end{aligned}, \tag{25}$$

showing itself to be unstable because of a double integrator cascade. The following acceleration dynamics

$$\begin{aligned} &\mathbf{y}_{ma}(z) = \mathbf{P}_a(z)\left(\mathbf{d}_a(z) + \mathbf{k}(\mathbf{q}, \Delta\boldsymbol{\omega}) + B_a\mathbf{u}(z)\right) \\ &\mathbf{y}_a(z) = \mathbf{y}_{ma}(z) + \mathbf{v}_a(z) + \partial\mathbf{P}_a(z)\mathbf{y}_{ma}(z) \end{aligned}, \tag{26}$$

is similar to (18) except for $\mathbf{k}(\mathbf{q}, \Delta\boldsymbol{\omega})$, which accounts for the first and second term in (20). In (26), the unknown disturbance $\mathbf{d}_a$ accounts for the non-gravitational spacecraft torques, namely magnetic and aerodynamic, and for the gradiometer bias $\mathbf{b}_a$. All other variables and $\mathcal{Z}$-transforms in (26) have similar meaning and expression as in (18). Note that $\mathbf{k}(\mathbf{q}, \Delta\boldsymbol{\omega})$ does not need to be explicitly separated from $\mathbf{d}_a$ when gradiometer measurements are employed, because of their wide frequency-band as already noted in Section 1.1.2. For this reason, $\mathbf{k}(\mathbf{q}, \Delta\boldsymbol{\omega})$ is represented with dashed lines in Fig. 3 and Fig. 8. Since ignoring $\mathbf{k}(\mathbf{q}, \Delta\boldsymbol{\omega})$ either in (25) or in (26) corresponds to perturb the Embedded Model with a structured uncertainty, closed-loop stability must be proved as it will be done in Section 1.1.7.

1.1.5. Attitude measurements

The attitude $\mathbf{q}$ is measured as the error between the predicted LORF quaternion $\hat{\mathcal{Q}}_O$ - the reference - and the inertial attitude quaternion $\mathcal{Q}_S$, the latter being provided by a pair of star trackers in cold redundancy.Denoting quaternion product and conjugate with $\otimes$ and $*$, and the attitude measurement vector with $\mathbf{y}_q$, wyields

$$\begin{aligned} &\left[1 \quad \mathbf{y}_q^T(i)/2\right]^T = \hat{\mathcal{Q}}_O^*(i) \otimes \mathcal{Q}_S(i) \\ &\mathbf{y}_q(i) = \mathbf{q}(i) + \mathbf{e}_q(i), \ \mathbf{e}_q(i) = \mathbf{v}_q(i) + \partial\mathbf{P}_q \cdot \mathbf{q}(i) \end{aligned}, \tag{27}$$

upon definition of the attitude measurement error $\mathbf{v}_q$ as follows

$$\begin{aligned} &\mathbf{v}_q(i) = \mathbf{v}_s(i) - \hat{\mathbf{e}}_O(i) \\ &\left[1 \quad \hat{\mathbf{e}}_O^T/2\right]^T = \mathcal{Q}_O^* \otimes \hat{\mathcal{Q}}_O \end{aligned}. \tag{28}$$

In (27), $\mathbf{e}_q$ is the model error and $\partial\mathbf{P}_q$ the neglected dynamics, mainly due to thrusters. In (28), $\mathbf{v}_s$ is the instrument noise and bias, while $\hat{\mathbf{e}}_O$ is the LORF prediction error. In principle, angular drag-free and attitude control may be achieved through attitude measurements alone. In practice, star-tracker noise prevents a wider bandwidth for disturbance estimation, and makes impossible to achieve the drag-free requirements of Table 1. That is especially true in the mission bandwidth $\mathcal{F}_1$, where gradiometer contribution is compulsory. On the contrary, gradiometer drift, entering drag-free commands, would force the long-term attitude to become unbounded with respect to the orbital frame, in the absence of attitude control. Gradiometer and star-tracker data fusion is therefore a key issue in attitude control design (Canuto, 2010).

3.5. Perturbing torques and aerodynamic stability

A deeper analysis of the perturbing torques, showing the degree of aerodynamic stability in the absence of attitude control, may be of interest. GOCE aerodynamic torques may be approximated 'in the small' (Bak & Wisniewski, 1996), i.e. for small perturbations around $\underline{\mathbf{q}} = 0$, as

$$\mathbf{c}_d(\mathbf{q}) \simeq -p(h)\left(\left(A_y a_y - A_x a_x\right) q_z \mathbf{k} + \left(A_z a_z - A_x a_x\right) q_y \mathbf{j}\right), \tag{29}$$

where $p(h) = 0.5\rho(h)V^2 C_D$ is the thermosphere pressure, $\rho(h) \approx 0.1\times10^{-9}$ kg/m^3 is the thermosphere density depending on solar activity and geodetic height h, and $C_D \simeq 2$ is the drag coefficient mainly established by surface properties. A_c, $c = x, y, z$, denotes the front, lateral and top surface areas of the main cylindrical body, while $a_c > 0$ denotes a pressure centre coordinate in the body frame. Aerodynamic stability 'in the small' occurs if $A_y a_y - A_x a_x > 0$ and $A_z a_z - A_x a_x > 0$. GOCE cylindrical shape and mass distribution lead to weak stability 'in the small', incapable of balancing the destabilizing gravity gradient in (20). Stability is recovered 'in the large' by tail fins. Consider the nonlinear version of (29), not reported here, and drop cross and first-order trigonometric terms, which are negligible because of the spacecraft shape. The aerodynamic torque 'in the large' is written as

$$\mathbf{c}_d(t) \simeq -p(h)\left(A_t a_{tx} |s_y| s_y \mathbf{j} + A_s a_{sx} |s_z| s_z \mathbf{k}\right), \tag{30}$$

where $s_c = \sin q_c$, and A_s and A_t denote areas of solar panels and tail fins, respectively, whereas $-a_{sx}$, $a_{sx} > 0$ and $-a_{tx}$, $a_{tx} > 0$ are the pressure-centre coordinates, corresponding to a pressure centre located behind the spacecraft CoM. The pitch component can now balance the gravity gradient due to a large pitch angle q_y, namely

$$\mathbf{c}_g(t) \simeq -\frac{J_x}{2}\Omega_{gx}^2 \sin(2q_x)\mathbf{i} + \frac{J_y}{2}\Omega_{gy}^2 \sin(2q_y)\mathbf{j}, \tag{31}$$

and prevent excessive increase of the drag cross-section, thus allowing a margin of a few days to orbit decline. Fig. 7 shows the composition of significant aerodynamic and gravity gradient torques 'in the large' ($|q_c| \le \pi/2$). The mere aerodynamic pitch component is shown for comparison. As Fig. 7 shows, equality of pitch components in (30) and (31) establishes a pair of stable equilibria, left and right of the unstable $q_y = 0$, defined by

$$q_y \simeq \pm\tan^{-1}\left(3J_y\omega_O^2\left(\rho C_d V^2 A_t a_{tx}\right)^{-1}\right). \tag{32}$$

By setting $|q_y| \le \pi/4$ and $a_{tx} \le L_x/2 \simeq 2.5$ m, the tail-fin area becomes bounded from below as $A_t \ge 0.7$ m^2, which is very close to actual value. Here we are only inter-

ested in the zero-pitch unstable equilibrium, to be stabilized by attitude control.

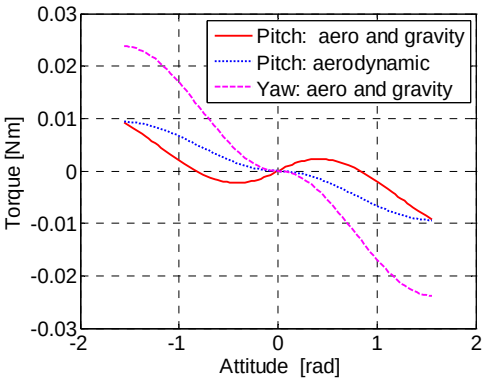

Fig. 7 Aerodynamic and gravity-gradient torques versus attitude.

3.6. Actuator dynamics and noise

The DFAC requirements in Table 1 can only be met by employing electric or low-noise gas propulsion.

1) A pair of ion thrusters (Edwards, Wallace, Tato & van Put, 2004), in cold redundancy, counteracts the along-track drag in a frequency band from DC to mission bandwidth.
2) An ensemble of m micro-thrusters, either electrical or cold-gas, counteracts the cross-axis drag components and tracks the reference attitude. Due to criticalities in micro-thruster technology, they were abandoned in favour of magnetic attitude control, implying acceptable degradation of angular requirements, but uncontrolled lateral motion (Sechi, Andrè, Andreis & Saponara, 2006). Here reference is made to micro-thrusters as they are essential for future drag-free missions (Silvestrin, 2005).

Let us split the thrust command vector

$$\mathbf{u}^T = \begin{bmatrix} u_t & \mathbf{u}_m^T \end{bmatrix} \tag{33}$$

into the command u_t of the active ion thruster and the command vector $\mathbf{u}_m$ of the micro-thrusters. By neglecting their dynamic response to be part of $\partial\mathbf{P}_l$ and $\partial\mathbf{P}_a$ in (18) and (26), because of settling times $< T$, a static thrust-to-acceleration relation may be written, depending on thruster geometry, scale factor and noise:

$$\begin{bmatrix} \mathbf{f}/m_s \\ \hline J^{-1}\mathbf{c} \end{bmatrix} = \begin{bmatrix} f_x/m_s \\ \hline \mathbf{f}_{yz}/m_s \\ \hline J^{-1}\mathbf{c} \end{bmatrix} = \begin{bmatrix} a_x \\ \hline \mathbf{a}_m \end{bmatrix} = B\left(\begin{bmatrix} u_t \\ \hline \mathbf{u}_m \end{bmatrix} + \begin{bmatrix} w_t \\ \hline \mathbf{w}_m \end{bmatrix} \right). \tag{34}$$

In (34) the thruster force $\mathbf{f}$ defined in (15) has been split into along-track and lateral components f_x and $\mathbf{f}_{yz}$. Propulsion noise is accounted for by w_t and $\mathbf{w}_m$. Matrix B in (34) may be rearranged for future use as follows:

$$B = \begin{bmatrix} B_l \\ \hline B_a \end{bmatrix} = \left[\begin{array}{c|c} b_x & \Delta B_m \\ \hline \mathbf{b}_{yz} & B_{myz} \\ \hdashline \mathbf{b}_a & B_{ma} \end{array}\right] = \left[\begin{array}{c|c} b_x & \Delta B_m \\ \hline \mathbf{b} & B_m \end{array}\right], \tag{35}$$

where B_l and B_a refer to CoM drag-free and attitude control, as defined in (18) and (26), respectively, and $\dim B_m = (2n-1)m$. The entries of matrix B in (35) depend on mass, inertia and thruster geometry. Some entries are negligible, especially ΔB_m coupling $\mathbf{u}_m$ to along-track acceleration a_x. On the contrary, entries coupling ion thrusters to lateral and angular accelerations are not negligible, because of their slanted orientation with respect to $\mathbf{i}$.

Equation (34) must be accompanied by thrust and thrust-rate bounds, not reported here. Since thruster noise adds to drag and torques, it must be compatible with control requirements in Table 1. Adequate bounds on the spectral density of the thruster noise have been derived and partly demonstrated by actual technology. Among these bounds, a stringent requirement concerns micro-thruster noise: the relevant spectral density should stay below the micro-Newton in the mission bandwidth and above.

4. Drag-free and attitude control design

4.1. Guidelines and block-diagram

Digital control is designed and implemented around the Embedded Model in the form of Control Laws, implementing state-to-command feedback, and Noise Estimators, implementing output-to-state feedback. The underlying theory may be found in Canuto (2007a). Control Laws are essentially model-based in their structure and tuning. Noise Estimators are model-based in their structure but plant-based in their tuning. The block-diagram is shown in Fig. 8.

Drag-free and attitude control parallels the Embedded Model decomposition.

1) Coordinate decomposition derives from decoupled CoM and attitude dynamics (12) and (25), and requires the $2n$ entries of the commanded accelerations a_x and $\mathbf{a}_m$ in (34) to be independently computed. Interaction only occurs when dispatching $\mathbf{a}_m$ to micro-thruster command $\mathbf{u}_m$. That amounts to finding a pseudo-inverse of B, which is obtained by solving the propellant saving problem (7) as explained in Section 5.2.
2) Hierarchical decomposition is permitted by gradiometer measurements capable of ensuring wideband disturbance cancellation. Residual accelerations due to accelerometer drift are either free-acting on the spacecraft centre-of-mass or contrasted by the attitude loop. This implies two pairs of Noise Estimators as in Fig. 8: one pair, $\mathbf{L}_r$ and $\mathbf{L}_l$, refers to position dynamics, the other pair, $\mathbf{L}_q$ and $\mathbf{L}_a$, refers to attitude. In both cases, the former estimator, having narrower bandwidth, retrieves the noise of the residual accelerations, whereas the latter one, having wider bandwidth, retrieves the noise of the rejected disturbance.

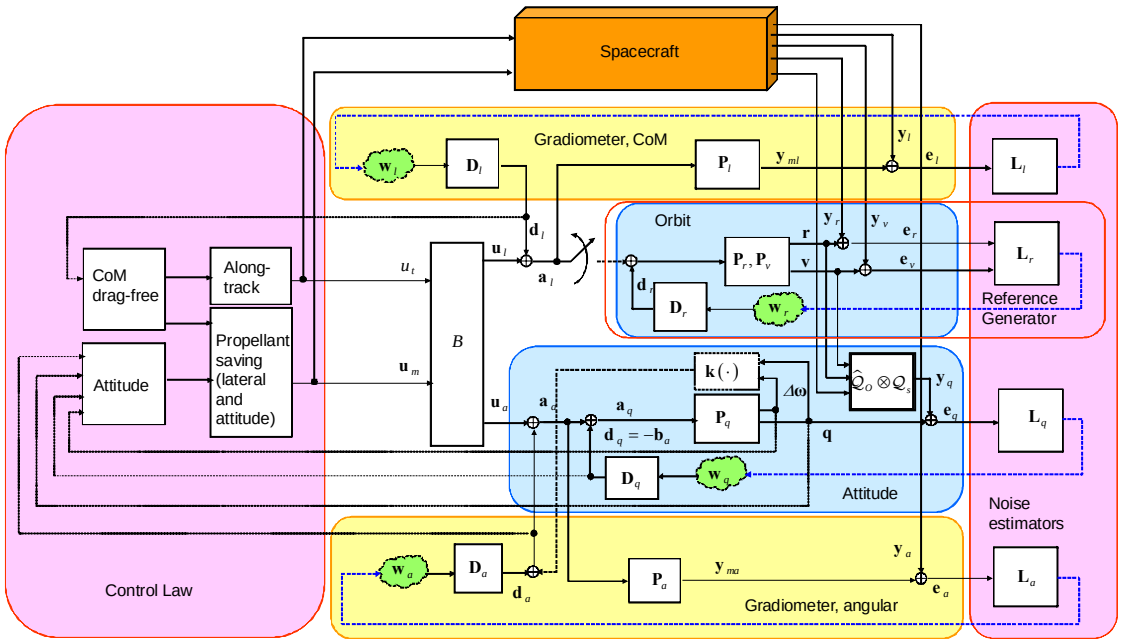

Fig. 8 Block-diagram of the Embedded Model surrounded by Control Law and Noise Estimators.

4.2. *Control Law*

Hierarchical decomposition entails three different sets of Control Laws, two of them actuating CoM and angular drag-free control, and a third one actuating attitude control. Drag-free control follows from (18), (26) and (35), by expressing residual accelerations as the following command/disturbance combinations

$$\begin{bmatrix} a_{lx} \\ \mathbf{a}_{lyz} \\ \mathbf{a}_a \end{bmatrix}(z) = \begin{bmatrix} b_x & 0 \\ \mathbf{b}_{yz} & B_{myz} \\ \mathbf{b}_a & B_{ma} \end{bmatrix} \begin{bmatrix} u_t \\ \mathbf{u}_m \end{bmatrix}(z) + \begin{bmatrix} d_{lx} \\ \mathbf{d}_{lyz} \\ \mathbf{d}_a \end{bmatrix}(z), \tag{36}$$

and by forcing them to zero according to (6). Note that $\mathbf{k}(\Delta\boldsymbol{\omega}, \mathbf{q})$ has been hidden in $\mathbf{d}_a$, as anticipated in Section 1.1.4. Then, by denoting the one-step predicted disturbance with the mark ^, CoM and angular drag-free Control Law follows:

$$u_t(z) = -\hat{d}_{lx}(z) / b_{tx}, \tag{37}$$

$$\begin{bmatrix} B_{myz} \\ B_{ma} \end{bmatrix} \mathbf{u}_m(z) = \\ = \begin{bmatrix} \mathbf{F}_{yz}(z) & 0 \\ 0 & I \end{bmatrix} \left(- \begin{bmatrix} \mathbf{b}_{yz} \\ \mathbf{b}_a \end{bmatrix} u_t(z) - \begin{bmatrix} \hat{\mathbf{d}}_{lyz} \\ \hat{\mathbf{d}}_a \end{bmatrix}(z) + \begin{bmatrix} 0 \\ \mathbf{c}_q \end{bmatrix}(z) \right). \tag{38}$$

The dynamic operator $\mathbf{F}_{yz}$ in (38) is a high-pass filter cancelling lateral low-frequency components, so as to bound micro propulsion (Section 5.2). Equation (38) is a set of $2n-1$ linear equations with m unknowns, the components of $\mathbf{u}_m(i)$, which can be solved through a pseudo-inverse B_m^{-1} which is solution of (7). It should be noted that the variables in (37) and in (38) are one-step predictions in view of delayed command actuation, which implies that disturbance prediction excludes noise components and only includes state variables, so as to respect the causality constraint.

The task of the attitude command $\mathbf{c}_q$ in (38) is to cancel, with the help of star tracker data, the gradiometer drift $\mathbf{b}_a$ from gradiometer prediction $\hat{\mathbf{d}}_a$, and therefore to keep the attitude bounded. To this end, the following Control Law, which is the composition of attitude and rate tracking errors, $-\hat{\mathbf{q}}$ and $-\Delta\hat{\boldsymbol{\omega}}$, respectively, and of the drift prediction $\hat{\mathbf{d}}_q$, can be shown to be adequate:

$$\begin{aligned} \mathbf{c}_q(z) &= -\left(K_1 \hat{\mathbf{q}}(z) + K_2 \Delta\hat{\boldsymbol{\omega}}(z)\right) T^{-2} - \hat{\mathbf{d}}_q(z) = \\ &= -\mathbf{C}(z) T^{-2} \hat{\mathbf{q}}(z) - \hat{\mathbf{d}}_q(z) \end{aligned}, \tag{39}$$

where

$$\begin{aligned} \mathbf{C}(z) &= K_1 + K_2 (z-1) \\ K_j &= \mathrm{diag}\{k_{jx}, k_{jy}, k_{jz}\},\ j = 1,2 \end{aligned}. \tag{40}$$

In (39), coordinate decomposition simplifies the feedback matrices K_1 and K_2 to be diagonal. Moreover, since attitude requirements in Table 1 are coordinate-independent, the values of K_1 and K_2 ensue from tuning n sets $\Lambda_c = \{1-\gamma_c, 1-\gamma_c\}$ of equal closed-loop eigenvalues.

4.3. Noise Estimators

Four noise vectors $\mathbf{w}_h$, driving the actual realizations of each disturbance class, must be estimated from sensor measures. According to hierarchical decomposition, the available $5n$ sensor measures may be decoupled as follows.

1) Drag Noise Estimator: $\mathbf{w}_l$ and $\mathbf{w}_a$ are estimated from the linear and angular gradiometer measurements $\mathbf{y}_l$ and $\mathbf{y}_a$.
2) Drift Noise Estimator: $\mathbf{w}_q$ is estimated from attitude measurement $\mathbf{y}_q$.
3) Gravity Noise Estimator: $\mathbf{w}_r$ is estimated from the CoM position and velocity measurements $\mathbf{y}_r$ and $\mathbf{y}_v$. Orbit dynamics in (12), together with the gravity Noise Estimator, provides the LORF prediction $\hat{\mathcal{Q}}_O$ and plays the role of the attitude Reference Generator.

Consider the drag Noise Estimator and restrict attention to a single axis, either linear or angular, keeping the subscript h and dropping c. The estimator is obtained by considering the thruster-to-gradiometer model comprising the series $\mathbf{P}_h \cdot \mathbf{D}_h$, which includes the second-order disturbance dynamics $\mathbf{D}_h$ from (13) and the controllable dynamics $\mathbf{P}_h(z) = z^{-1}$ from (16). The series is observable from y_h and the relevant $\mathcal{Z}$ transform holds:

$$\mathbf{P}_h(z)\mathbf{D}_h(z) = z^{-1}\begin{bmatrix} 1 & (z-1)^{-1} & (z-1)^{-2} \end{bmatrix}. \tag{41}$$

The Noise Estimator is a static feedback from the model error $\bar{e}_h = y_h - \hat{y}_{mh}$ as in the steady-state Kalman filter, since $\dim \mathbf{w}_{hc} = 3$ is the same as the order of the series in (41). This implies

$$\bar{\mathbf{w}}_h(z) = L_h \bar{e}_h(z),\ L_h^T = \begin{bmatrix} l_{h0} & l_{h1} & l_{h2} \end{bmatrix}. \tag{42}$$

The gains in L_h ensue from tuning the closed-loop eigenvalue set $\Lambda_h = \{1-\beta_h, 1-\gamma_h, 1-\gamma_h\}$, where the second pair has been set equal for simplicity's sake.

In the following, closed-loop and sensitivity $\mathcal{Z}$-transforms will be employed, namely $\mathbf{V}_h(z) = \hat{y}_{mh}(z)/y_h(z)$ and $\mathbf{S}_h(z) = 1 - \mathbf{V}_h(z)$. More specifically, low- and high-frequency asymptotes are used, namely

$$\begin{aligned} &\mathbf{V}_{h0}(z) = \lim_{z-1\to 0} \mathbf{V}_h(z) = 1 \\ &\mathbf{V}_{h\infty}(z) = (z-1)^{-2}\left(2\gamma_h\beta_h + \gamma_h^2\right), \end{aligned} \tag{43}$$

and

$$\begin{aligned} &\mathbf{S}_{h\infty}(z) = \lim_{z-1\to\infty} \mathbf{S}_h(z) = 1 \\ &\mathbf{S}_{h0}(z) = (z-1)^2 \frac{1 + 2\gamma_h/\beta_h}{\gamma_h^2} = \frac{(z-1)^2}{(2\pi f_{h0} T)^2}, \end{aligned} \tag{44}$$

where f_{h0} approximates the sensitivity bandwidth. In (43), care must be taken concerning $z-1 \to \infty$; this implies that an asymptote of $\left|\mathbf{V}_h\left(e^{j2\pi fT}\right)\right|$ exists in the frequency domain $f < f_{\max}$, but progressively folds as $f \to f_{\max}$.

Unlike the drag estimator (42), the drift estimator cannot be a static feedback, since the series

$$\mathbf{P}_q(z)\mathbf{D}_q(z) = T^2(z-1)^{-2}\begin{bmatrix} 1 & (z-1)^{-1} & (z-1)^{-2} \end{bmatrix}, \tag{45}$$

has order $n_q = 4$ greater than $\dim \mathbf{w}_q = 3$. The simplest dynamic feedback can be shown to be first-order and equal to

$$\begin{aligned} &\bar{\mathbf{w}}_q(z) = \mathbf{L}_q(z)\bar{e}_q(z) \\ &\mathbf{L}_q(z) = L_q + (z-1+\beta_q)^{-1} L_{qq} \\ &L_q^T = \begin{bmatrix} l_q & 0 & 0 \end{bmatrix},\ L_{qq}^T = \begin{bmatrix} l_{q0} & l_{q1} & l_{q2} \end{bmatrix} \end{aligned}, \tag{46}$$

having denoted the attitude model error with $\bar{e}_q = y_q - \hat{y}_{mq}$ (Canuto 2007a). In (46), only n_q nonzero gains in L_q and L_{qq} are necessary, in addition to pole β_q, to freely tune the $n_q + 1$ closed-loop eigenvalues of the set $\Lambda_q = \{1-\gamma_q, ...\}$, in which, for simplicity's sake, all entries are equal. Coming to the asymptotes of the closed-loop transfer functions, as in (43), the following holds

$$\begin{aligned} &\mathbf{V}_{q\infty}(z) = 20(z-1)^{-3}\gamma_q^3\left(\gamma_c/\gamma_q\right) \\ &\mathbf{S}_{q0}(z) = 4(z-1)^4\gamma_q^{-4}\left(1 + 2\left(\gamma_q/\gamma_c\right)^2\right), \end{aligned} \tag{47}$$

where, because of causality, the Control Law pole γ_c enters equation (47). The same condition does not occur in (43) because drag-free laws (37) and (38) are restricted to disturbance rejection.

Finally, because the series $\mathbf{P}_r \cdot \mathbf{D}_r$ has order $n_r = 4$ greater than $\dim \mathbf{w}_r = 3$, the gravity estimator should be in principle a dynamic feedback, as the drift estimator. Instead, a static feedback can be designed by exploiting GPS range and rate measurements $\mathbf{y}_r$ and $\mathbf{y}_v$.

4.4. Robust stability and performance

1.1.6. Introduction

Let us restrict considerations to attitude stability and performance. Denote the generic attitude with q and the generic acceleration with a_q, which according to (25) are related by $q = \mathbf{P}_{qc} \cdot a_q$. Combining (25) and (26) with (38) and (39) leads to

$$\begin{aligned} &q_y(z) = \hat{e}_q(z) + \mathbf{S}_c(z) \times \\ &\times\left(\mathbf{P}_{qc}(z)\left(d_a(z) - \hat{d}_a(z) + d_q(z) - \hat{d}_q(z)\right) - \hat{e}_q(z)\right), \end{aligned} \tag{48}$$

where $\hat{e}_q = q - \hat{q}$ is the attitude prediction error and $\mathbf{S}_c = \left(1 + \mathbf{C}_c(z)\mathbf{P}_{qc}(z)T^{-2}\right)^{-1}$ is the Control Law sensitivity. Now since $\hat{e}_q$ depends on the disturbances d_a and d_q, and on the model error e_q defined in (27), the expression converts to

$$q(z) = -\mathbf{V}_q(z)e_q(z) + \mathbf{S}_q(z)\mathbf{P}_q(z)\left(d_q + d_a - \hat{d}_a\right)(z), \tag{49}$$

where $\mathbf{S}_q$ is the attitude sensitivity reported in (47) and $\mathbf{V}_q = 1 - \mathbf{S}_q$ the complementary function. The drag-free residual $d_a - \hat{d}_a$ depends on the drag sensitivity $\mathbf{S}_h$ in (44) ,for $h = a$, through the following relation

$$d_a(z)-\hat{d}_a(z)=\mathbf{S}_a(z)\left(d_a-d_q\right)(z)\,. \tag{50}$$

Combining (49) and (50) yields the final expression

$$\begin{aligned} q(z)&=-\mathbf{V}_q(z)e_q(z)+\\ &+\mathbf{S}_q(z)\mathbf{P}_q(z)\left(\mathbf{V}_a(z)d_q(z)+\mathbf{S}_a(z)d_a(z)\right)\end{aligned}\,. \tag{51}$$

1.1.7. Closed-loop stability versus structured uncertainty

The closed-loop system comprising the Embedded Model, free of modelling errors, Control Laws and Noise Estimators can be shown to be internally stable if and only if the n^2 predictor eigenvalue sets Λ_{hc} and the n Control Law sets Λ_c lie inside the unit disk. Since part of the model in (26), namely the destabilizing term $\mathbf{k}(\Delta\boldsymbol{\omega},\mathbf{q})$, has been hidden in the unknown disturbance $\mathbf{d}_a$, closed-loop stability should be proved. Consider the pitch angle q_y, and separate d_a from $k_y(\Delta\boldsymbol{\omega},\mathbf{q})=\Omega_{gy}^2 q_y$ in (51), thus obtaining

$$\begin{aligned}\left(1-\mathbf{S}_q(z)\mathbf{P}_q(z)\mathbf{S}_a(z)\Omega_{gy}^2\right)q_y(z)&=-\mathbf{V}_q(z)e_q(z)+\\ &+\mathbf{S}_q(z)\mathbf{P}_q(z)\left(\mathbf{V}_a(z)d_q(z)+\mathbf{S}_a(z)d_a(z)\right)\end{aligned}\,. \tag{52}$$

Then, assuming that the RHS in (52) is bounded and attitude-independent, in other words that is free of neglected dynamics, the sufficient stability condition ensues:

$$\max_{|f|\le f_{\max}}\left|\mathbf{S}_q(jf)\mathbf{P}_q(jf)\mathbf{S}_a(jf)\Omega_{gy}^2\right|<1\,. \tag{53}$$

To be rather conservative, assume $|\mathbf{S}_q|=1$ and, exploiting the low-frequency approximation (44), write $|\mathbf{S}_a|=(f/f_{a0})^2$. Then, by expressing $|\mathbf{P}_q|$ with the help of (25) as $|\mathbf{P}_q|=(2\pi f)^{-2}$, inequality (53) converts to

$$2\pi f_{a0}>\Omega_{gy}\simeq\omega_O\,, \tag{54}$$

which places a loose lower limit on the drag predictor eigenvalues. The above inequality fully justifies dropping $\mathbf{k}(\Delta\boldsymbol{\omega},\mathbf{q})$ from (26), at least when gradiometer measurements are available.

1.1.8. Plant stability recovery and performance

When the generic measure $\mathbf{y}_h(i)$ comes from spacecraft sensors, assumptions guaranteeing model-based stability cease to be valid because of modelling errors $\partial\mathbf{P}_h$. Their effect spills through sensor measurements, making the performance variables $\mathbf{a}$, $\dot{\boldsymbol{\omega}}$ and $\mathbf{q}$ self-dependent through the uncertain dynamics $\partial\mathbf{P}_h$. By restricting considerations to a single axis and approximating neglected dynamics to being linear and time-invariant, the generic attitude q can be written, partly omitting z and the subscript c, as

$$\begin{aligned}\left(1+\mathbf{V}_q\cdot\partial\mathbf{P}_q+\mathbf{S}_q\cdot\mathbf{V}_a\cdot\partial\mathbf{P}_a\right)q(z)&=\\ =-\mathbf{V}_q v_q(z)+\mathbf{S}_q\cdot\mathbf{P}_q\cdot\left(\mathbf{V}_a d_q(z)+\mathbf{S}_a d_a(z)\right)&\end{aligned}\,. \tag{55}$$

Equation (55) descends from (51) by correcting the unit factor in the left-hand side (LHS) with a combination of the neglected dynamics and by replacing the model error e_q with the measurement noise v_q, in the RHS. In (55), $\partial\mathbf{P}_q$ accounts for neglected thruster dynamics and $\partial\mathbf{P}_a$ for thruster-to-gradiometer dynamics. The LHS in (55) is responsible for closed-loop stability. The RHS, only dependent on the driving and measurement noise $\mathbf{w}_h$ and $\mathbf{v}_h$, is responsible for performance.

Stability, performance assessment and design may start from (55) and develop either in the time or in the frequency domain. The latter domain is pursued here as being more suitable to robust stability and DFAC requirements shown in Table 1. To this end, several inequalities are derived from (55) and simplified according to their frequency region of validity.

1) The robust stability inequality which descends from the RHS of (55) corresponds to small gain theorem (Canuto, 2007a). By neglecting $|\mathbf{V}_{q\infty}\partial\mathbf{P}_q|$ in (55) because of the narrower bandwidth of the attitude state-predictor, and by assuming the peak of $|\partial\mathbf{P}_a(f)|_{\mathrm{L}1}$ to occur at $f=f_\partial$, above the bandwidth $f_a\simeq(2\pi T)^{-1}\gamma_a$ of $\mathbf{V}_a$, the inequality simplifies to

$$|\mathbf{V}_{a\infty}(f_\partial)||\partial\mathbf{P}_a(f_\partial)|\le\eta<1\,. \tag{56}$$

2) Making explicit the high-frequency asymptote

$$|\mathbf{V}_{a\infty}(f_a)|\simeq(2\pi f_\partial T)^{-2}\left(2\gamma_a\beta_a+\gamma_a^2\right) \tag{57}$$

computed in (43), converts (56) into an inequality, in which the discrete-time poles β_a and γ_a related to the bandwidth of $\mathbf{V}_a$ explicitly enter as follows

$$\begin{aligned}&\alpha_\eta\beta_a\gamma_a\left(1+0.5\gamma_a^2/\beta_a\right)\le\eta<1\\ &\alpha_\eta=(2\pi f_\partial T)^{-2}|\partial\mathbf{P}_a(f_\partial)|\le 0.2\end{aligned}\,. \tag{58}$$

3) A drag-free inequality for the mission bandwidth $\mathcal{F}_1$ can be derived by applying (55) to the acceleration a_q defined in (25). To this end, (56) is assumed to reach a feasible degree of robustness $\eta<1$ and f_a to lie above $\mathcal{F}_1$. Then, replacing each disturbance in (55) with the relevant spectral density, and assuming the second-order spectral density $S_d(f)=S_{d0}(2\pi fT)^{-2}$ of drag forces (see Section 1.1.2) to dominate accelerometer and star-tracker errors yields

$$|\mathbf{S}_{a0}(f)|S_d(f)\le(1+\eta)\underline{S}_{a1}(1+\sigma_1)\,. \tag{59}$$

where $\underline{S}_{a1}$ is the acceleration bound in the mission bandwidth $\mathcal{F}_1$ reported in Table 1 and $|\sigma_1|<1$ residuals due neglected spectral densities.

4) Moreover, by replacing $\mathbf{S}_{a0}(f)$ in (59) with the low-frequency asymptote

$$|\mathbf{S}_{a0}(f)|\simeq(2\pi fT)^2\gamma_a^{-2}(1+2\gamma_a/\beta_a) \tag{60}$$

as computed in (44), a second inequality, which is explicit in the closed-loop poles, is obtained

$$\gamma_a^2 \geq \alpha_1^2 \left(1+2\gamma_a/\beta_a\right)\left(1+\varphi_1(\eta)\right),\ \alpha_1 \simeq 0.035\,, \qquad (61)$$

where $\varphi_1(\eta)$ must satisfy $|\varphi_1(\eta)|<1$ in view of feasibility.

5) By proceeding thus, other inequalities can be obtained which are explicit in the poles of the attitude state-predictor, namely γ_q in (47), and in the Control-Law pole γ_c. They are written as

$$\begin{aligned} &\gamma_q^4 \geq \alpha_2^4 \left(1+2\left(\gamma_q/\gamma_c\right)^2\right)\left(1+\varphi_2(\eta)\right),\ \alpha_2 \simeq 0.0005 \\ &\gamma_q^3 \leq \alpha_3^3 \left(\gamma_q/\gamma_c\right)\left(1+\varphi_3(\eta,\gamma_a)\right),\ \alpha_3 \simeq 0.0015 \end{aligned}\,, \qquad (62)$$

where the former derives from attitude requirements at lower frequencies and the latter from the mission-bandwidth requirements. The terms $|\varphi_k|$, $k=2,3$ must be sufficiently less than unit as in (61).

Inequalities (58) to (62) can be solved by treating $\eta<1$, $\beta_a \leq 1$ and γ_q/γ_c as tuneable parameters. That leads them to provide upper and lower bounds $\gamma_{h,\min}$ and $\gamma_{h,\max}$ to state-predictor poles γ_h, $h=a,q$. Inequalities become feasible as soon as

$$\gamma_{h,\min}(\eta,\ldots) \leq \gamma_{h,\max}(\eta,\ldots)\,. \qquad (63)$$

Interestingly, feasibility requires two key conditions.

1) The attitude Control Law must have a wider bandwidth than the attitude state-predictor, which corresponds to $\gamma_q/\gamma_c<0.05$ in agreement with Canuto (2007a).
2) The drag-free bandwidth f_a must be close to $f_{\max}$, which ensures $|\varphi_3(\eta,\gamma_a)|<1$ in (62) and supersedes (61) with a tighter inequality in agreement with the hierarchical decomposition in Section 4.1. The condition in turn requires drag-free Noise Estimator and Control Law to be an internal loop of the attitude control.

The CoM drag-free control is only concerned with inequalities (58) and (61). Table 2 shows designed and simulated eigenvalues for the different laws.

Table 2. Designed and simulated eigenvalues and relevant bandwidths

Dynamics	Law	Discrete-time poles γ_h			BW [Hz]	Degree of robustness η
		Size	Design	Simulation		
Nyquist frequency					5	
CoM, x	Noise Estimator	2	0.24÷0.4	0.3	0.5	< 0.1
		1	1	0.7		
CoM, y,z each axis	Noise Estimator	2	0.18÷0.4	0.2	0.3	< 0.1
		1	1	0.6		
Attitude – each axis	Control Law	2	0.01	0.01	0.016	< 0.1
	Drag-free Noise Estimator	2	0.18÷0.4	0.2	0.3	
		1	1	0.6		
	Attitude Noise Estimator	3	$(0.4\div0.5)\times10^{-3}$	0.0005	<0.001	
		2		0.001		

5. Simulated results and discussion

5.1. *Drag-free and attitude control performance*

Fig. 9 shows the spectral densities of the residual CoM accelerations under conservative spacecraft/environment conditions. They are compared to the target bound defined in Table 1. The target bound is met with a margin from the mission bandwidth $\mathcal{F}_1$ to $f_{\max}$. The along-track margin appears to accommodate drag doubling to cope with increased solar activity. The low-frequency jump is due to gradiometer bias. Only lateral accelerations (out-of-plane and radial, dotted in Fig. 9) look slightly across the bound at low frequencies, which is the cost to be paid for thrust restraining, though acceptable to science. As a matter of fact, lateral acceleration of the actual GOCE will be free running, owing to micro-propulsion forsaking (Sechi, Andrè, Andreis & Saponara, 2006).

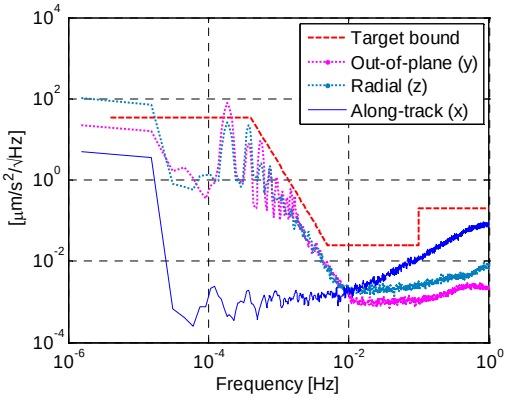

Fig. 9 Spectral densities of the residual CoM accelerations compared to target bound.

Fig. 10 compares attitude, angular rate and acceleration to target bounds. The results refer to roll q_x. Target bounds are respected with a margin, despite the conservative star-tracker noise and bias, manifesting itself in the flat spectral profile in the low-frequency region.

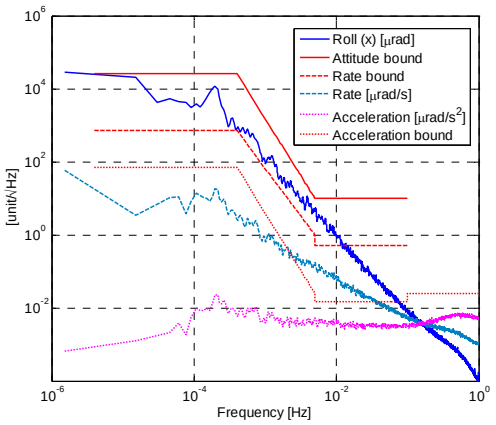

Fig. 10 Spectral densities (top to bottom) of attitude (roll), rate and angular acceleration compared to target bounds.

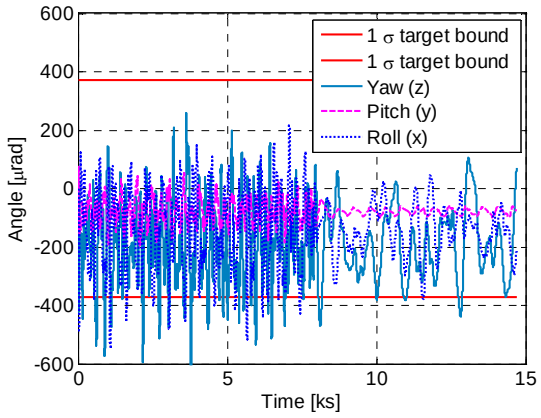

Fig. 11 Attitude angles from fine pointing to science mode.

Fig. 11 shows the time history of roll, pitch and yaw during a pair of control modes and compares them to 1 σ target bound, centered on zero attitude. Note the [ks] time unit has been employed. Attitude is controlled without gradiometer measurements up to 80 ks, but from star-tracker data alone (the so-called fine-pointing mode). From 80 ks onwards, the so-called DFAC or science mode, gradiometer data are employed. The difference is immediate, since the fine-pointing attitude appears noisier than the science mode, as expected. Note, however, that the overall RMS is not very different, as the gradiometer only helps filtering star-tracker noise from the mission bandwidth $\mathcal{F}_1$. All attitude angles are clearly biased, as the worst-case star-tracker misalignment has been simulated. The smaller range of the pitch angle q_y is due to a weaker star-tracker noise along that axis. Random fluctuations are tuned to the orbital frequency (0.2 mHz) because of the narrow bandwidth (< 1 mHz) of the attitude state-predictor. During fine pointing, gradiometer may be either ON or OFF. Whether ON, the significant offset of the angular acceleration may be estimated, thus providing the initial state of $\mathbf{d}_q$ in (25).

5.2. *Propellant saving and thrust peak restraining*

As mentioned in Section 1, cold gas thrusters require propellant saving, electric thrusters require peak restraining. Although these strategies are alternative, both of them have been implemented so as to add their benefits. To this end, peak restraining is not implemented as a linear programming, but by filtering out the low-frequency components of the lateral command forces. Propellant saving is more complex, as linear programming must be solved at each control step i, in order to provide the optimal basic solution, or in other words, the optimal quintuple $p(i)$ of thrusters to be fired. It is well known linear programming provides a solution within a finite number of steps, close to $2n$ in the average, but since only fixed times shorter than T are admitted in control units, invariant algorithms and constant iteration size are preferable. The solution, briefly mentioned in the Appendix, takes advantage of the duality properties of the basic solutions of (7), which in turn is favoured by micro-thruster layout.

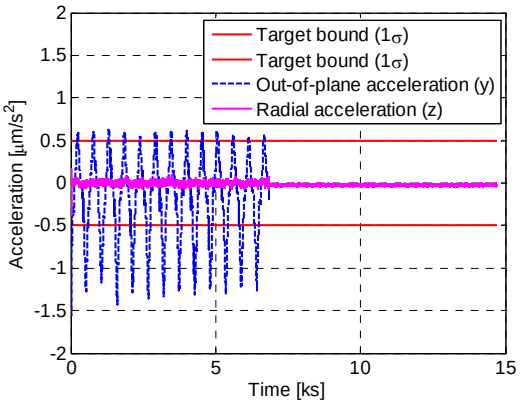

Fig. 12 Case 1. Time history of lateral accelerations.

Three cases are treated, from the worse to the better.

1) No filter is applied to lateral forces and commands are allocated to all thrusters (Fig. 12 and Fig. 14).
2) Linear programming is applied, corresponding to firing only five thrusters at a time.
1) Both the improving strategies, low-frequency filter and linear programming, are applied (Fig. 13 and Fig. 14).

Performance is shown in Fig. 12 to Fig. 14, and in Table 3. The figures show the time history of the lateral accelerations from fine pointing to science modes, as well as total and average thrust. In case 1, lateral accelerations are brought to zero during the science mode, from 80 ks onwards, at the cost of higher thrust peaks and higher consumption. In case 3, only the lateral components in the mission bandwidth are brought to zero (which cannot be seen from Fig. 13) with the benefit of reducing thrust peak and average to below 40 %. Note in Fig. 13 radial accelera-

tion increases from fine-pointing to science mode because of the slant ion-thruster orientation. Table 3 shows that a decisive contribution to average and peak reduction comes from avoiding low-frequency drag-free control of lateral forces, but that real-time linear programming saves about 25 % of propellant from case 1 to case 2.

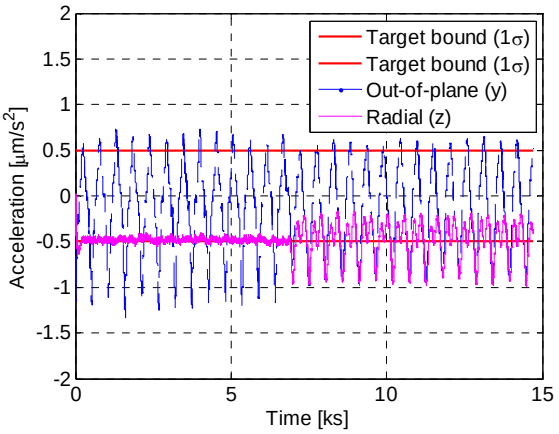

Fig. 13 Case 3. Time history of lateral accelerations.

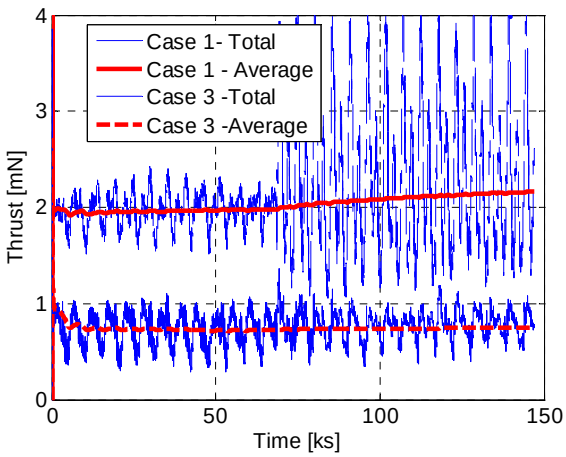

Fig. 14 Cases 1 and 3. Total and average micro-propulsion thrust.

Table 3. Performance of thrust allocation strategies

Case	Strategy		Ion thruster [mN]		Micro-thrusters [mN]	
	Peak restraint	Propellant saving	Average	Peak	Total average	Single thruster peak
1	None	Constant	9.85	19.1	2.32	1.01
2	None	Linear programming	9.85	19.1	1.77	0.92
3	Filter	Linear programming	9.85	19.1	0.77	0.39

6. Conclusions

Six-axis spacecraft control with multivariate sensors and actuators has been solved and performance demonstrated through fine simulation. The control code, written in C language, was included in the end-to-end simulator of the GOCE prime contractor and was the maquette for final code development. Control algorithms have been developed around the Embedded Model, discrete-time state equations including detailed disturbance dynamics for a total of more than fifty state variables. Control laws play the role of sensor-to-EM and EM-to-actuator interfaces, to be designed either as static or dynamic feedback channels. Sensor-to-EM feedback channels - the Noise Estimators - are univocally defined by the driving noise, and must be be carefully designed as the sole way to update the disturbance state in real time. Feedback gains, especially those of the Noise Estimators, are computed to guarantee performance and, at the same time, robust stability in the presence of neglected dynamics. A simplified yet effective procedure is reported leading to values that need to be refined through simulation and commissioning, but that are neatly related to requirements and expected perturbations.

Acknowledgements

The author is indebted to reviewers for their helpful suggestions and remarks, and to G. Sechi, Thales Alenia Space Italia, Turin, Italy, for helpful discussions. Part of the work was done under a grant from the GOCE prime contractor, Thales Alenia Space Italia, Turin, Italy.

References

Aguirre-Martinez, M., & Cesare, S. (1999) GOCE mission concept, error deviation and performances. *Bollettino di Geofisica Teorica e Applicata, 40* (3-4), 295-302.

Bak, T., & Wisniewski R. (1997). Passive aerodynamic stabilization of a Low Earth Orbit satellite. *Proc. 3rd Int. ESA Conf. on Spacecraft Guidance, Navigation and Control Systems*, Noordwijk, The Netherlands (pp. 469-474), ESA SP-381.

Bertotti, B., & Farinella P. (1990). *Physics of the Earth and the Solar System*. Dordrecht (The Netherlands): Kluwer Academic Pu.

Canuto, E., Bona, B., Calafiore G., & Indri, M. (2002). Drag-free control for the European satellite GOCE. Part I: modelling. Part II: digital control. *Proc. 41st IEEE Conf. Dec. and Control,* Las Vegas, Nevada (pp. 1269-1274, 4072-4077).

Canuto, E., Martella, P., & Sechi, G (2003). Attitude and drag control: an application to the GOCE satellite. *Space Science Reviews, 108* (1-2), 357-366.

Canuto E. (2007a). Embedded Model Control: outline of the theory. *ISA Trans., 46* (3), 363-377.

Canuto, E. (2010). Drag-Free Control of the GOCE satellite: noise and observer design. *IEEE Trans. on Control Systems Technology*, *18* (2), 501-509.

Canuto, E., Massotti, L., & Santos M. (2007). Local orbital frame observer for LEO drag-free satellites. *Preprints of the 17th IFAC Symp. on Automatic Control in Aerospace*, Toulouse, France (Session FR-02).

Donati, F., & Vallauri M. (1984). Guaranteed control of 'almost-linear' plants. *IEEE Trans. on Automatic Control, 29* (1), 34-41.

Edwards, C. H., Wallace, N. C., Tato, C., & van Put P. (2004). The T5 ion propulsion assembly for drag compensation on GOCE. *Proc. 2nd Int. GOCE User Workshop*, Frascati, Italy, ESA SP-569.

Fichter, W., Gath, P., Vitale, S., & Bartoluzzi D. (2005). LISA Pathfinder drag-free control and system implications. *Class. Quantum Grav.*, *22* (10), S139-S148.

Fritsche, B., & Klinkrad, H. (2004). Accurate prediction of non-gravitational forces for precise orbit determination. Part I: Principles of the computation of coefficients of forces and torques. *Proc. of the AIAA/AAS Astrodynamics Specialist Conference and Exhibit,* Providence, Rhode Island (Paper AIAA 2004-5461).

Haines, R. (2000). Development of a drag-free control system. *Proc. 14th Annual AIAAA/USU Conf. on Small Satellites*, Logan, Utah (Session VII, No. 2).

Kaplan, E. D. ed. (1996). *Understanding GPS: Principles and Applications*. Boston: Artech House Publishers.

Luenberger, D. G. (1973). *Introduction to linear and nonlinear programming*. Reading (Massachussetts): Addison Wesley.

Picone, J. M., Hedin, A. E., Drob, D. P., & Aikin, A. C. (2002). NRLMSISE-00 empirical model of the atmosphere: Statistical comparisons and scientific issues. *J. Geophys. Res.*, *107* (A12), 1468-1483.

Prieto, D., & Ahmad, Z. (2005). A drag-free control based on model predictive technique. *Proc. 2005 American Control Conference*, Washington, DC (USA), Vol. 3, (pp. 1527-1533).

Scheeres, D. J. (1998). The restricted Hill four-body problem with applications to the Earth-Moon-Sun system. *Celestial Mechanics and Dynamical Astronomy*, *70* (2), 75-98.

Sechi, G., Andrè, G., Andreis, D., & Saponara M. (2006). Magnetic attitude control of the GOCE satellite. *Proc. 6th Int. ESA Conf. on Spacecraft Guidance, Navigation and Control Systems*. Loutraki, Greece (pp. 37-43), ESA SP-606.

Silvestrin, P. (2005). Control and navigation aspects of the new Earth observation missions of the European Space Agency. *Annual Reviews in Control*, *29* (2), 247-260.

Touboul, P., Rodrigues, M., Willemenot, E., & Bernard, A. (1996) Electrostaic accelerometers for the equivalence principle test in space. *Class. Quantum Grav.*, *13*, A67-A78.

Vaillon, L., Borde, J., Duhamel, T., & Damilano, P. (1996). Drag-free control systems and technologies, *Space Technol., 16* (5-6), 245-254.

Wertz, J. R. ed. (1985). *Spacecraft attitude determination and control*. Dordrecht (The Netherlands): D. Reidel Pu.

Ziegler, B., & Blanke, M. (2002). Drag-free motion control of satellite for high-precision gravity field mapping. *Proc. 2002 IEEE International Conference on Control Applications*, Glasgow, Scotland (UK) (pp.292-297).

Appendix A. Real-time linear programming

Consider a basis B_k, $k = 0,...,2^5 - 1 = M - 1$ of the matrix B_m in (35), corresponding to selecting a quintuple p_k of thrusters, such that $\operatorname{rank} B_k = 5$. The linear-programming tableau (Luenberger, 1973) can be shown to be of the following sort for any k

$$\left[\begin{array}{c|c|c} I & C_k & \mathbf{u}_k \\ \hline 0 & \mathbf{r}_k & -c_k \end{array}\right],\ \mathbf{r}_k = \begin{bmatrix} 0 & 4 & 4 \end{bmatrix},\ C_k = \begin{bmatrix} 1 & -1 & -1 \\ 0 & -1 & 0 \\ -1 & 0 & 0 \\ 1 & -1 & -1 \\ 0 & 0 & -1 \end{bmatrix}, \quad (64)$$

where $\mathbf{r}_k \geq 0$ is the relative cost, $\mathbf{u}_k$ is the basic solution, c_k is the dual cost and C_k lists the non-basic columns. Since only the column order in C_k and $\mathbf{r}_k$ may change, the dual solution $\mathbf{e}_k = \begin{bmatrix} 1 & 1 & 1 & 1 & 1 \end{bmatrix}$, which is always the same for any k, is dually feasible for any k. Given a primal non-feasible solution $\mathbf{u}_k$, i.e. one having negative rows, it is then possible to find a new basis B_h and a new quintuple p_h, still dually feasible, which increases the dual cost $c_k = \mathbf{e}_k \mathbf{u}_k$. The key point of the algorithm is that the basis-updating mechanism is made a priori and saved. In other words, any basic quintuple p_k univocally corresponds to an ordered set $\mathcal{P}_k = \{p_{k1},..., p_{k5}\}$ of quintuples, each for any column to be replaced. The algorithm starts at any step i from the previous quintuple $p_k(i-1)$ and basis $B_k(i-1)$, and computes, according to (7) the candidate thrust $\mathbf{u}_0(i) = B_k(i-1)^{-1} \mathbf{a}_m(i)$. When the latter is nonnegative, i.e. primal and feasible, the procedure stops; otherwise, the most negative component is detected in $\mathbf{u}_0(i)$ and a new quintuple is selected from $\mathcal{P}_k$. The procedure continues for a fixed number of steps, $\nu \leq 4$, to guarantee fixed computing time. In the rare occurrence of the last iteration $\mathbf{u}_{\nu-1}(i)$ not being feasible, the negative components, of the amplitude of thrust noise, may be allocated among all thrusters.

Enrico Canuto was born in Varallo (Piemonte), Italy. He received a Degree in Electrical Engineering from Politecnico di Torino, Turin, Italy, where he joined the staff as Associate Professor of Automatic Control in 1983. From 1982 to 1997 he contributed to data reduction of the European astrometric mission Hipparcos. Technological studies in view of scientific and drag-free space missions, like Gaia and GOCE provided the opportunity of applying Embedded Model Control to drag-free satellites and to electro-optics. He contributed to the conception, design and implementation of the interferometric thrust-stand Nanobalance, capable of sub-micro-Newton accuracy. His research interests cover all the entire field of control problems that are challenging because of complexity, uncertainty and precision.